Experiments in Fluids (2019) 60:42
https://doi.org/10.1007/s00348-019-2689-2

RESEARCH ARTICLE

Two-phase flow measurements of an unsteady breaking bore

Xinqian Leng[1] · Hubert Chanson[1]

Received: 12 November 2018 / Revised: 24 January 2019 / Accepted: 25 January 2019

Abstract

A key feature of breaking bores, jumps, and spilling breakers is the roller region, characterised by intense shear and recirculation, associated with air bubble entrainment and splashing. Detailed unsteady air–water flow measurements were conducted in a breaking bore propagating in a large-size channel, using an array of dual-tip phase-detection probes and an ultra-high-speed video camera. The results showed a steep roller front, with a very-dynamic air–water bubbly region, albeit with a relatively limited air–water roller region. In this study, a major challenge was the inconsistency in light intensity linked to the travelling nature of the bore. A simple flow visualisation technique was applied to retrieve the two-dimensional side-looking profile of the roller edge and average void fraction. The results were validated independently with a phase-detection probe. While the probe data lacked spatial variability, the study reinforces the needs of high-quality validation data set, including in unsteady transient flows.

1 Introduction

A key feature of breaking bores, jumps, and spilling breakers is the roller region (Lubin and Chanson 2017). The roller is a highly turbulent flow motion characterised by intense shear and recirculation, associated with air bubble entrainment, splashing, and spray and energy dissipation (Tricker 1965; Hoyt and Sellin 1989). Historically, the roller properties were investigated visually (Tricker 1965), using a quasi-steady breaker (Duncan 1981; Cointe and Tullin 1994; Coakley et al. 2001), and in stationary hydraulic jumps (Rajaratnam 1962; Chanson and Brattberg 2000; Misra et al. 2006).

Recent developments in two-phase gas–liquid measurement techniques provided comprehensive data sets in steady flows (Wood 1991; Chanson 2013). State-of-the-art reviews encompassed Jones and Delhaye (1976), Cartellier and Achard (1991), as well as Chanson (2002, 2016) in air–water flows. While the processing of most instruments is relatively simple in steady flows, the literature on unsteady two-phase flow measurements is limited, except for a relatively small number of experiments in wave breaking (e.g., Hwung et al. 1992; Hoque and Aoki 2005), cavitating pseudo-periodic flows (Stutz and Reboud 1997, 2000), dam break wave (Chanson 2004, 2005), and positive surge (Leng and Chanson 2015a). Most data sets delivered limited information on the gas–liquid flow properties, and none of these reported data in a shock flow, except for the dam break wave and surge studies.

During the present work, new unsteady air–water flow measurements were undertaken in a breaking bore. The unsteady experiments were performed in a relatively large-size flume. Unsteady two-phase flow properties were recorded using an array of phase-detection probes, complemented by non-intrusive observations based on ultra-high-speed video movies and acoustic displacement meter signals, to comprehend the wave breaking dynamics, the roller's air–water flow structure, and its basic gas–liquid properties.

2 Experimental facility, instrumentations, and experimental procedure

2.1 Experimental facility

The experimental flume was 19 m-long 0.7 m-wide, with a PVC bed and 0.5 m high glass sidewalls (Fig. 1). The bed slope was adjustable and set to 0.75% for the experiments.

Electronic supplementary material The online version of this article (https://doi.org/10.1007/s00348-019-2689-2) contains supplementary material, which is available to authorized users.

✉ Hubert Chanson
h.chanson@uq.edu.au

[1] School of Civil Engineering, The University of Queensland, Brisbane, QLD 4072, Australia

Published online: 14 February 2019

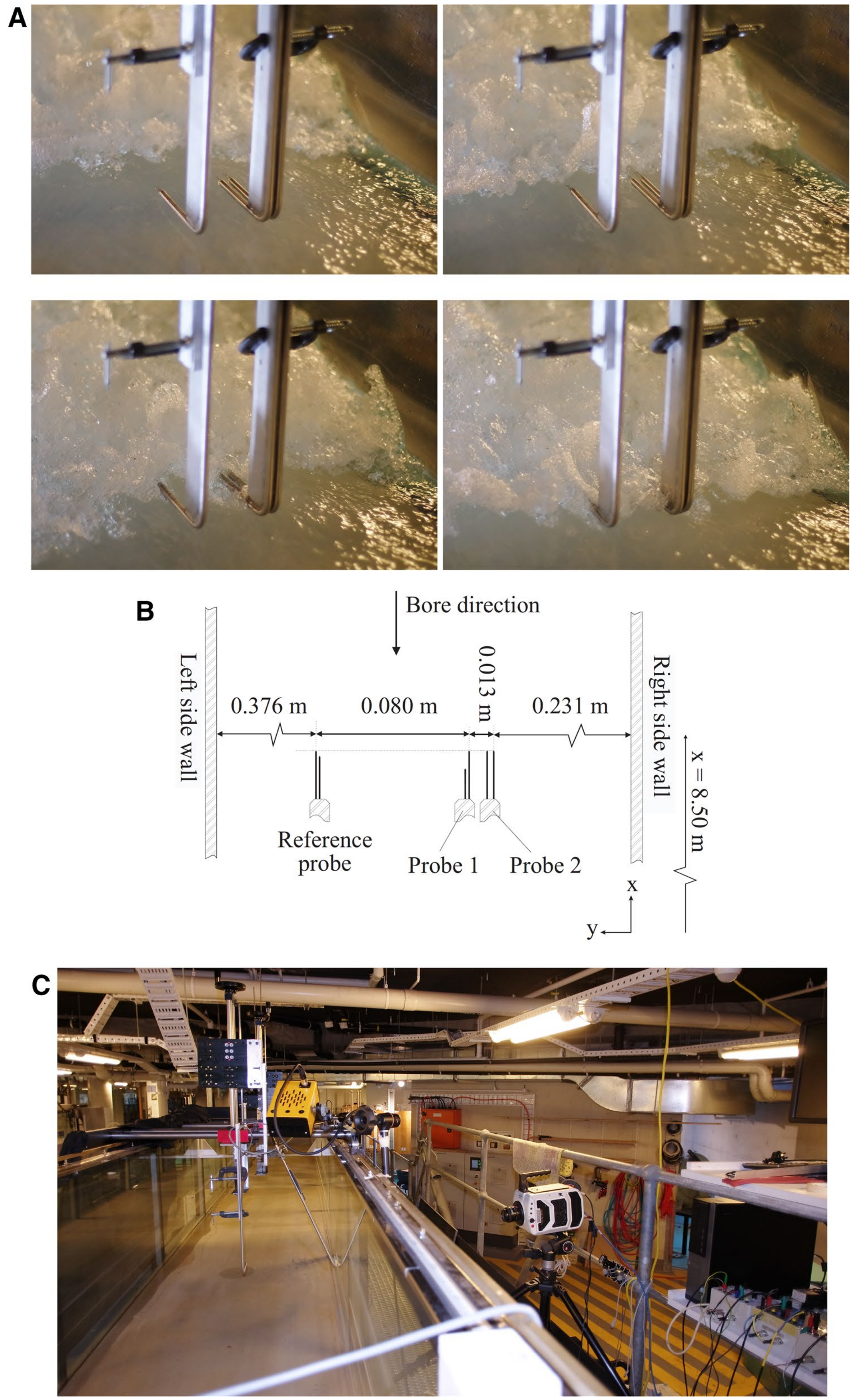

Fig. 1 Experimental flume and instrumentation. **a** Breaking bore roller propagating, from top left to bottom right, past the phase-detection probe array—shutter speed: 1/2000 s—from left to right, top to bottom: 0.12 s between photographs. **b** Dimensioned sketch and general view in elevation of the phase-detection probe array positioned about the channel centreline. Initially, steady-flow direction from bottom to top; bore propagation from top to bottom. **c** Looking downstream, with the reference probe on the channel centreline, a dual-tip phase-detection probe next to the right sidewall, and the ultra-high-speed video camera on the right

The same channel was previously used by Leng and Chanson (2015a) and Leng (2018). The water flow was supplied by an upstream intake tank equipped with flow calming devices and flow straighteners, followed by a smooth three-dimensional convergent, leading to the 19 m-long flume. At the channel's downstream end, a rapidly closing gate was installed. Figure 1a, c shows general views of the experimental flume and generated bore. "Appendix 1" presents two high-speed video sequences.

2.2 Instrumentation

The discharge was measured by a magneto flow meter with an accuracy of 10^{-5} m^3/s. The unsteady water depths were recorded with a series of acoustic displacement meters Microsonic™ Mic + 25/IU/TC positioned above the channel at $x = 17.41$ m, 9.96 m, 8.50 m, and 6.96 m, where x is the longitudinal distance from the flume's upstream end. All acoustic displacement meters (ADMs) were calibrated against point gauge measurements in steady flows and sampled at 200 Hz during the unsteady bore experiments.

The air–water flow properties were recorded using three dual-tip phase-detection probes located at $x = 8.50$ m. That is, the leading sensor of each probe was located at $x = 8.50$ m. Each dual-tip probe was equipped with two needle sensors, developed at the University of Queensland. The inner electrode (Ø = 0.25 mm) was made of silver (99.99% purity), with 24 µm PTFE insulation coating. The outer electrode was a stainless-steel hypodermic needle (ID = 0.5 mm, OD = 0.8 mm). The two tips were mounted on a ∅8 mm tube housing the connectors and cables. Two probes were equipped a leading and trailing sensor, separated longitudinally by $\Delta x = 0.0027$ m and 0.0092 m. One probe, located about the channel centreline (Fig. 1a, b, left probe), was used as a reference, using the same approach as Chanson (2004, 2005) in a dam break wave. Its position remained unchanged for the entire duration of the experiments: $x = 8.50$ m, $y = 0.324$ m, and $z = 0.105$ m, where y is the transverse distance from the right sidewall and z is the vertical elevation measured above the channel bed. The other probe (Probe 1) was placed with its leading sensor at the same longitudinal position (and vertical elevation) as the sensors of Probe 2. The third probe (Probe 2) was equipped with two identical sensors separated transversally by $\Delta y = 0.0037$ m. All sensors were aligned with the longitudinal direction, facing downstream and designed to pierce the bubbles/droplets in the bore roller (Fig. 1a). The probe sensors were excited simultaneously by an electronic system (Ref. UQ82.518) designed with a response time less than 10 µs. The sampling rate was 20 kHz or 100 kHz per sensor for all probes. Figure 1a shows the probe array arrangement with the three probes about the channel centreline, and Fig. 1b presents a dimensioned schematic.

Observations through the glass sidewalls were recorded using a Phantom ultra-high-speed digital camera (v2011) (Fig. 1c) equipped with a Nikkor 50 mm *f*/1.4 lens, producing images with a small degree (~ 1.3%) of barrel distortion. The camera system was able to record up to 22,700 monochrome frames per second (fps) in high definition or 1,000,000 frames per second in low-definition (128 × 16 pixels). In the present study, the movies were recorded at 20,000 fps in high definition (1280 × 800 pixels). The camera exposure time was set between 10 and 17 µs. The video movies were analysed manually to guarantee maximum reliability of the data. The camera was positioned at $x = 8.5$ m beside the right glass sidewall facing the phase-detection probe (Fig. 1c). The observation window was 64 cm wide and 40 cm long, while the depth of field was less than 20 mm and focused slightly inside the right glass sidewall. The observations were two-dimensional, and three-dimensional patterns would not be typically recorded.

In addition, high-resolution dSLR photography was undertaken with prime lenses, producing images with an absolutely negligible degree of barrel distortion. Further details on the experimental facility and instrumentation were reported by Leng and Chanson (2018).

2.3 Experimental procedure

The measurements were performed in a breaking bore with a Froude number:

$$Fr_1 = \frac{U + V_1}{\sqrt{g \times d_1}} = 2.2 \tag{1}$$

where g is the gravity constant, d_1 is the initial water depth, U is the bore celerity positive upstream, and V_1 is the initial cross-sectional averaged velocity; all the initial flow conditions being measured at $x = 8.5$ m (Fig. 1a). The initial steady-flow conditions were $Q = 0.10$ m^3/s, $d_1 = 0.097$ m and $V_1 = 1.49$ m/s. The bore was generated by the fast gate closure at the downstream end of the channel. The closure time was less than 0.2 s, and did not affect the generation and upstream propagation of the bore. All the experiments were conducted with Brisbane tap water.

In the first series of measurements, the phase-detection probe array was positioned about the channel centreline, as shown in Fig. 1a, b (also Movie bore_probe_test8.avi, "Appendix 1"). In the second series of experiments series, the dual-tip phase-detection Probe 1 was positioned close to the sidewall (Fig. 1c), and its signal outputs were recorded synchronously with the ultra-high-speed speed camera. For each series, the reference probe (Fig. 1a, left probe) was always set at the same longitudinal, transverse, and vertical location, and it was used as time reference.

During each experimental run, the phase-detection probes were recorded synchronously with the acoustic displacement meters and ultra-high-speed camera. The centreline measurements were conducted at 33 vertical elevations. At a few positions on the centreline and next to the sidewall, the measurements were repeated between 5 and 50 times, and ensemble-averaged.

3 Signal processing (1): phase-detection probes

3.1 Presentation

In a turbulent flow motion, the instantaneous velocity is often decomposed into a time-average component plus a turbulent fluctuation component:

$$V = \overline{V} + v \tag{2}$$

where V is the instantaneous velocity, $\overline{V}$ is the time-averaged velocity, and v is the instantaneous velocity fluctuation. Equation (2) is called a Reynolds decomposition (Schlichting and Gersten 2000). When the flow motion is unsteady, the time average is not physically meaningful. Relatively simple processing techniques may be applied to gradually varied unsteady flow and periodic flows, e.g., low-pass filtering or phase-averaging (Piquet 1999; Cox and Shin 2003; Kimmoun and Branger 2007). In a transient highly unsteady-flow motion, as in a breaking bore, the quantities of the mean motion must be determined by ensemble averaging (Bradshaw 1971; Schlichting and Gersten 2000; Chanson and Docherty 2012). The same experiment is repeated N times and the ensemble average is defined as follows:

$$\overline{V}(x, y, z, t) = \frac{1}{N} \times \sum_{j=1}^{N} V_j(x, y, z, t) \tag{3a}$$

When the number N of repeats is small, the ensemble-average may be better defined in terms of the ensemble-median value:

$$\overline{V}(x, y, z, t) = \text{Median}\left(V_j(x, y, z, t)\right)_{j=1,N} \tag{3b}$$

The turbulent velocity fluctuation v becomes the deviation of the instantaneous velocity V from the ensemble average $\overline{V}$ (Bradshaw 1971). In transient highly unsteady surge flows, sensitivity analyses showed that the number of repeats N must be at least equal to 20 to yield the accurate measurements of median free-surface properties, velocity component, and tangential stresses (Leng and Chanson 2015b, 2017).

3.2 Air–water flow characteristics

For all experiments, the time origin ($t = 0$) was selected when the leading sensor of the reference phase-detection probe first detected an air-to-water interface.

The outputs of the phase-detection probes were voltage signals recorded during the bore roller passage. Typical instantaneous signals are shown in Fig. 2a where the time origin ($t = 0$) corresponds to the first detection of an air-to-water interface by the leading sensor of the reference phase-detection probe, located at $z = z_{\text{ref}} = 0.105$ m. Figure 2a presents the instantaneous voltage signals recorded at four vertical elevations. In Fig. 2a, each vertical drop in signal corresponded to the detection of a water-to-air interface by the sensor, while each vertical rise corresponded to the detection of an air-to-water interface. Although the probe signal should be theoretically rectangular, the instantaneous signal is not exactly square because of the finite size of the tip, the wetting/drying time of the interface covering the tip, and the response time of the probe and electronics (Cartellier and Achard 1991; Chanson 2016). A single-threshold technique was used to convert the instantaneous voltage signals into instantaneous void fraction and to calculate bubble interfacial times. The single-threshold technique is a very robust method in free-surface flows, and the threshold was herein set at 50% of the air–water voltage range to cover the wide range of void fractions in the whole air–water flow column following Toombes (2002), Chanson (2002, 2016), and Felder and Chanson (2015). The output yields the instantaneous void fraction c, with $c = 1$ in air and $c = 0$ in water.

On the channel centreline, the measurements were conducted with the probe array (Probes 1 and 2) being positioned at 33 different vertical elevations within 0.095 m $< z <$ 0.255 m, while the reference probe position remained unchanged: $z = z_{\text{ref}} = 0.105$ m. The synchronised results provided the vertical distributions of instantaneous void fraction $c(z, t)$ at each time step t. Through a vertical integration, the data provided an instantaneous clear-water depth d:

$$\mathrm{d}(t) = \int_{z=0}^{z=+\infty} (1 - c(z, t)) \times \mathrm{d}z \tag{4}$$

The instantaneous clear-water depth d is comparable to the equivalent clear-water depth commonly used in high-velocity free-surface steady flows (Wood 1984, 1985; Chanson 1997), albeit the latter is calculated in terms of a time-averaged void fraction C_{mean}. The signal outputs were further analysed in terms of the number of air–water interfaces and air–water chord times (Leng and Chanson 2018). Herein, the air and water chord times were derived from the raw probe signal outputs using a single-threshold technique, with the threshold was set at 50% of the air and water voltages, since this setting is considered the most robust discrimination in high-velocity free-surface flows (Toombes 2002; Chanson 2016).

The air–water flow measurements were repeated 50 times at $z = 0.105$ m (reference probe) and 25 times at $z = 0.120$ m and 0.175 m (Probes 1 and 2). At a given vertical elevation z, the instantaneous ensemble-averaged void fraction C in the roller was calculated as follows:

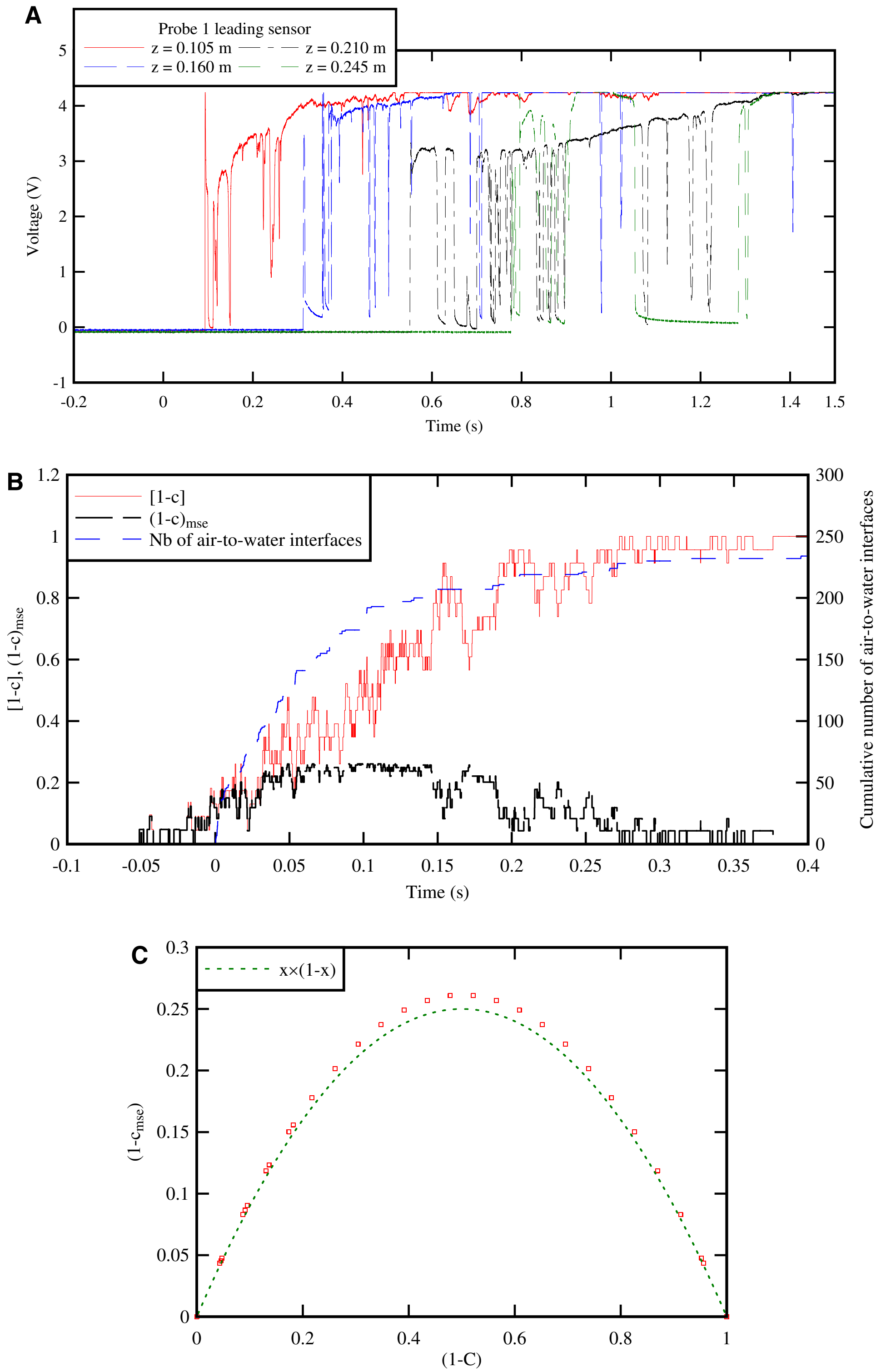

Fig. 2 Instantaneous probe voltage signal output, ensemble-averaged liquid fraction, and liquid fraction variance (mean-square error)—experimental conditions: $x = 8.50$ m, $Fr_1 = 2.2$, $d_1 = 0.097$ m, $z_{ref} = 0.105$ m, Probe 1, leading sensor. **a** Instantaneous voltage signals at several vertical elevations (single run data). **b** Time-variation of instantaneous ensemble-averaged liquid fraction and liquid fraction variance (mean-square error) (minimum of 10 repeats), and cumulative number of air-to-water interfaces (all 25 runs) at $z–z_{ref} = 0.015$ m. **c** Relationship between instantaneous ensemble-averaged liquid fraction and liquid fraction variance (mean-square error)—data at $z–z_{ref} = 0.015$ m—comparison with Eq. (7)

$$C(z,t) = \frac{1}{N} \times \sum_{j=1}^{N} c_j(z,t) \tag{5}$$

Typical data are presented as the instantaneous ensemble-averaged liquid fraction $(1 - C)$ in Fig. 2b (solid red curve). The difference between the third and first quartiles (C_{75}–C_{25}) characterised the instantaneous free-surface fluctuations. For a Gaussian distribution of the data, around its mean (C_{75}–C_{25}) would be equal to 1.3 times the standard deviation of the total ensemble (Spiegel 1972). Since the instantaneous void fraction c has a bi-modal distribution and $C_{75} \geq C_{25}$, the following result holds: $(C_{75}–C_{25}) = 0$ or 1.

For an ensemble of runs, the variance c_{mse} of the instantaneous void fraction is as follows:

$$c_{mse} = \frac{1}{N} \times \sum_{j=1}^{N} (c_j - C)^2 \tag{6}$$

where c is the instantaneous void fraction, C is the ensemble-averaged void fraction, and N is the number of repeats. Since the instantaneous void fraction is either 0 or 1: namely, $c = 1$ for a proportion of data equals to C, Eq. (6) yields the following (Murai et al. 2006; Chanson 2016):

$$c_{mse} = C \times (1 - C) \tag{7}$$

The relationship between ensemble-averaged void fraction and void fraction mean-square error (MSE) is thus parabolic, as shown in Fig. 2c.

The signal outputs were also analysed in terms of the number of air–water interfaces and air–water chord times. Figure 2b presents the time-variation of cumulative number of air-to-water interfaces detected during all 25 runs (dashed blue curve). The derivative of the cumulative number of air-to-water interfaces is comparable to the bubble count rate, i.e., the number of water-to-air interfaces detected per unit time. Note that the bubble count rate is implicitly equal to the water drop count rate in the upper roller region. Since the bubble count rate was low, the aerated flow region was small, and the sampling rate was high, a straight derivative of the raw cumulative number of air-to-water interfaces would be meaningless. The instantaneous cumulative number of air-to-water interfaces data was low-pass filtered before the derivative was calculated using central differences. The cut-off frequency was selected as F_{cutoff} = 50 Hz, although meaningful results were obtained for F_{cutoff} ≈ 20 to 50 Hz, based on a preliminary sensitivity analysis, as a compromise between the high bubble count rate next to the bore leading edge and the bubble detection rate in the downstream end of the roller.

3.3 Comment

When the bubble/droplet interfaces are successively detected by two probe sensors aligned along a streamline, the interfacial velocity may be calculated by an individual event method (Liu and Bankoff 1993; Chanson 2005) or by a cross-correlation technique (Herringe and Davis 1974; Jones and Delhaye 1976; Chanson 2002). Herein, both methods were applied without tangible results, and no interfacial velocity data could be derived.

A careful analysis of high-resolution high-shutter speed photographs and ultra-high-speed movies suggested that the first particles impacted the sensors in a quasi-random manner (Leng and Chanson 2018): that is, from all directions, as illustrated in the movie bore_probe_test8.avi ("Appendix 1"). There was no preferential particle direction corresponding to the phase-detection sensor alignment, i.e., horizontal longitudinal and horizontal transverse directions (Fig. 1a).

4 Signal processing (2): ultra-high-speed video camera

4.1 Presentation

Side-view video movies featuring the breaking roller of a propagating breaking bore were recorded in high definition (HD, 1280 × 800 pixels) at 22,000 fps, as illustrated in Fig. 3a and in the movie bore_side.avi ("Appendix 1"). When the bore arrived, the lighting of the video camera frame changed drastically, with the bore roller area lightened up because of the air bubble entrainment and associated light refraction. The water beneath the breaking roller and the air above the roller remained dark, enabling some post-processing of the video movies based on the lighting contrast between the air and water phases. One such information was the side profile of the roller outer edge and the position of roller toe. The roller toe is a flow singularity where air is entrapped and vorticity is generated (Hornung et al. 1995; Brocchini and Peregrine 2001; Wang et al. 2017) (Fig. 3a).

In the highly aerated breaking roller region, the light intensity was positively correlated to the amount of entrained air. Although the lighting conditions would change inevitably during the bore propagation, the pixel intensity at a given location may be related to the amount of aeration. Within a small number of frames during which the time interval was sufficiently small and the bore could be treated almost as quasi-stationary, the average pixel intensity across frames could be calibrated against the void fraction measured by the dual-tip phase-detection probes.

4.2 Side profile of a breaking bore roller

Major contributions to flow visualisations in air–water flows included Mossa and Tolve (1998) and Leandro et al. (2012), who quantified the vertical distribution of air entrainment in two-dimensional (2D) images of steady hydraulic jumps. The present study expanded upon the method of Leandro et al. (2012), by setting a threshold for pixel intensity between air and water. As illustrated in Fig. 3b, three distinctive regions can be seen along the vertical direction: (1) an air region above the outer edge of the roller, (2) the air–water flow region within the breaking roller, and (3) a clear-water region underneath. The three regions were separated by setting a pixel intensity threshold. Herein, a threshold of 50 was

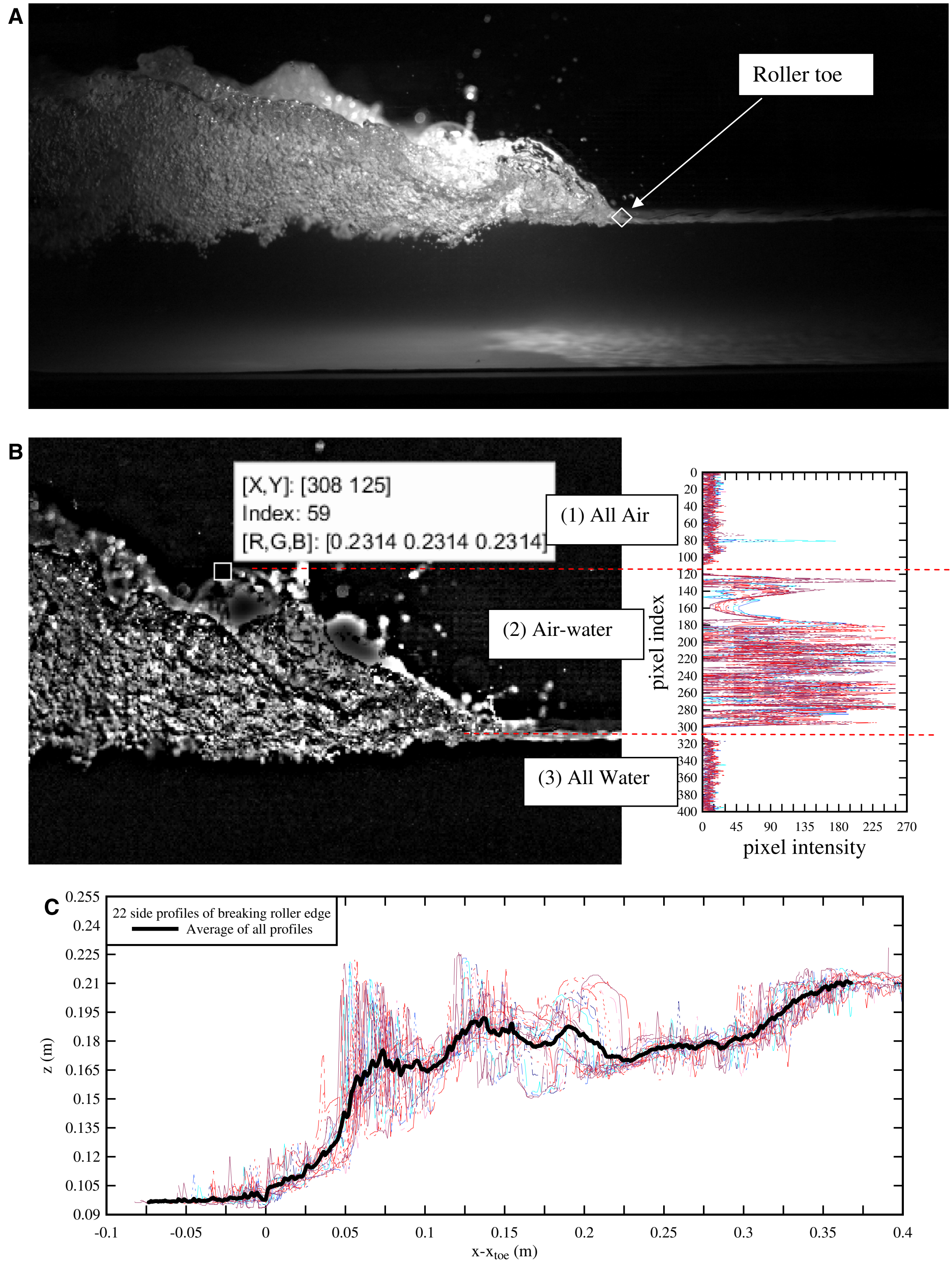

Fig. 3 Ultra-high-speed video camera image processing—flow conditions: $Q = 0.101$ m^3/s, $x = 8.50$ m, $\mathrm{Fr}_1 = 2.18$, $d_1 = 0.097$ m, $U = 0.64$ m/s, bore travelling from left to right. **a** Frame shot from the video series recorded by the ultra-high-speed video camera Phantom v2011 at 22,607 fps—side view through the left sidewall at $x \sim 8.5$ m, with bore propagation from left to right. **b** Gray-scale image (left) and pixel intensity of the roller at the vicinity of the toe (x–x_{toe} = 0.11–0.12 m) (right). **c** Ensemble-averaged instantaneous free-surface profile of the roller (22 runs)

applicable to separate regions (1) and (2), as well as regions (2) and (3), as shown in Fig. 3b (right).

The outer edge of the roller was determined as the first vertical index of the pixel that was associated with an intensity higher than 50, and the algorithm was applied frame-by-frame. The data were then smoothed using a non-overlapping window of 22 frames, yielding a time series of roller side profile with a time increment of 1 ms (i.e., 0.00097 s). Ensemble averaging was performed to the smoothed roller profiles (22 profiles) after synchronisation based on the position of the roller toe x_{toe}. Figure 3c shows typical ensemble-averaged results.

4.3 Liquid/void fraction in a propagating breaking bore

The ensemble-averaged void fraction in the breaking bore roller was quantified based on the processing of image's pixel intensity. The process consisted of two stages: (1) pre-processing of video frame data to remove the background noise and homogenise the lighting condition, and (2) post-processing of the pixel intensity with smoothing and ensemble averaging, to avoid random and extreme values. The pre-processing was done by batch processing using the same algorithm for each image. Figure 4a shows a typical frame shot, directly output from the high-speed video movie. The final output image is shown in Fig. 4b. After processing, the pixel intensity data of the entire sequence were smoothed using a non-overlapping window of 22 frames. Ensemble averaging was performed to the matrix of smoothed pixel intensity, after synchronising all data based on the position of the roller toe x_{toe}.

The present method was based on the assumption that, at a fixed longitudinal location where the lighting was consistent, the pixel intensity pi was proportional to the local void fraction (see discussion in "Appendix 2"). The relationship can be generalised as follows:

$$\mathrm{pi} = \begin{cases} 255 & \text{for } c = 1 \\ 0 - 255 & \text{for } 0 < c < 1 \\ 0 & \text{for } c = 0 \end{cases} \tag{8}$$

Plotted as a function of the vertical direction of the frame, the pixel intensity data showed two regions with low values, with their boundaries indicated by black arrows in Fig. 4c. For each longitudinal location $x–x_{toe}$, the transition between high and low pixel intensity above the roller edge was identified. After post-processing, the data were ensemble-averaged over five smoothed frames and the typical results are shown in Fig. 4d, with the vertical pixel index transformed into the vertical elevation z measured from the channel bed. The data showed overall a clear increase in pixel intensity with increasing vertical elevation at a given longitudinal location, as well as an increase in free-surface level as the longitudinal distance increased downstream of the roller toe.

4.3.1 Comparison to ensemble-averaged void fraction results from dual-tip phase-detection data

A validation data set was recorded to assess the output of the proposed video analysis technique. Ensemble-average measurements were performed using a phase-detection probe at six vertical elevations, with five repeats at each elevation. For the calibration and validation against the ultra-high-speed video data, the phase-detection probe signals were processed using a single-threshold technique, and two thresholds were used: 10% and 50% of the water-to-air voltage. The former was applied to account for the smallest air inclusions detected by the probe array. For completeness, a few early studies linked the threshold level to the local void fraction (Jones and Delhaye 1976). For example, Chanson et al. (2006) applied a 15% threshold level in plunging jet flows in seawater with very fine bubble sizes. The ultra-high-speed video camera output (pi) and phase-detection probe data (C) were compared at different longitudinal locations downstream of the roller toe ($x–x_{toe}$ = 0.05–0.3 m). Figure 5 shows a typical comparison, indicating a good agreement for both single-threshold values. A few differences were observed at lower vertical elevations for $x–x_{toe}$ = 0.1 and 0.2 m, where the phase-detection probe results using a 10% threshold gave slightly better comparison with the video data.

4.3.2 Remarks

One issue, found with all video movies irrespective of the settings, was the inconsistency in light intensity within the camera frame. Herein, the main challenge was the travelling nature of the bore, unlike, for example, a stationary hydraulic jump. When breaking, the bore entrapped a large amount of air bubbles, which constantly reflected and refracted lights in all the directions, causing a drastic change in lighting conditions, as the bore was travelling in the camera frame. Even with the most uniform initial lighting conditions, consistent lighting throughout frame could not be ensured once the bore arrived. It is acknowledged that uncertainty still exists, and the results may be biased by non-uniform background lighting.

5 Instantaneous and ensemble-averaged liquid fractions in the bore roller

5.1 Instantaneous liquid fraction and bore roller profile

The phase-detection probe array detected simultaneously the instantaneous void fraction at several elevations at the

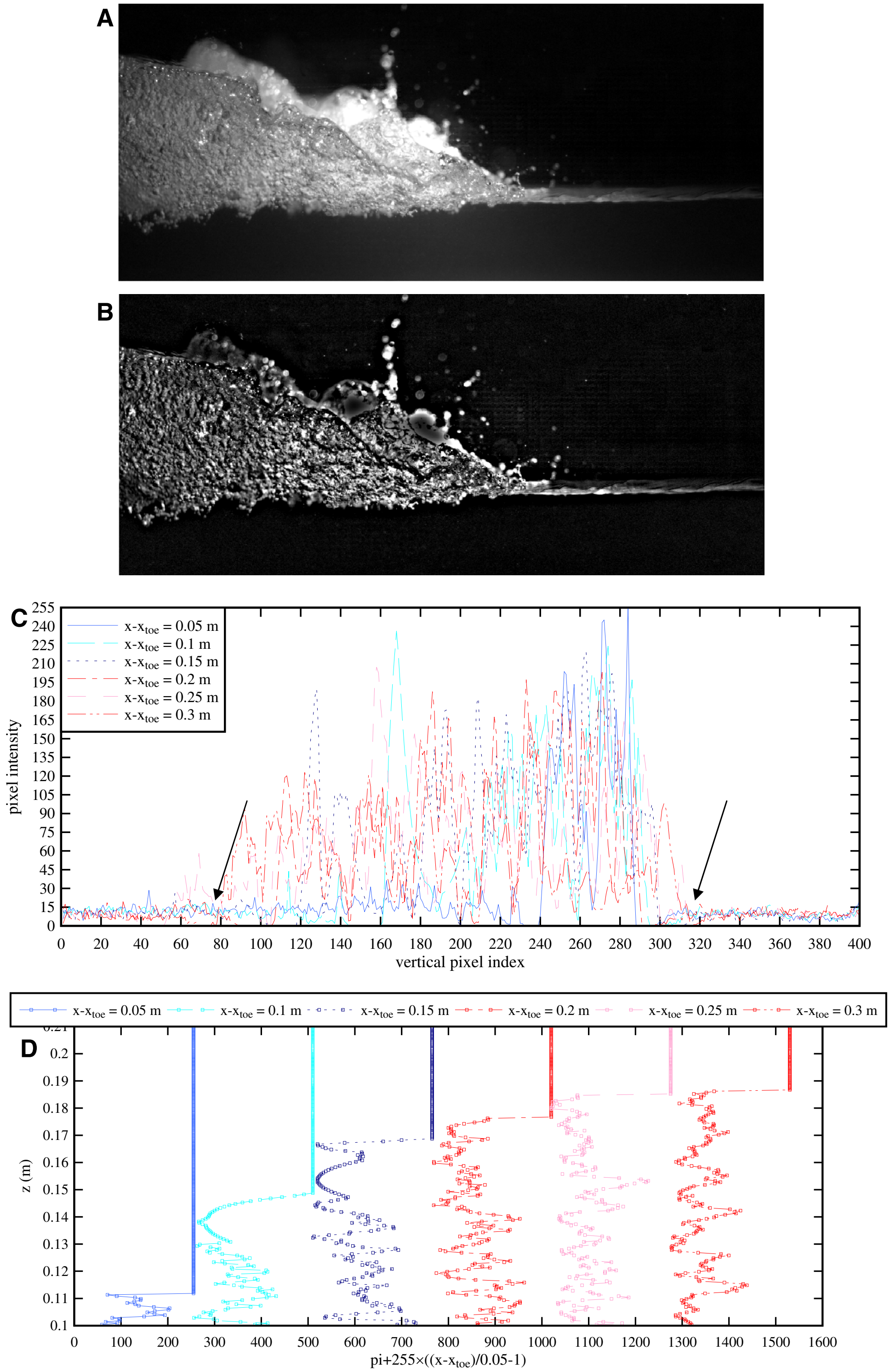

Fig. 4 Signal processing of ultra-high-speed camera data and vertical profiles of pixel intensity (pi) data at longitudinal locations downstream of the roller toe—flow conditions: $Q=0.101$ m^3/s, $x=8.50$ m, $\mathrm{Fr}_1=2.18$, $d_1=0.097$ m, and $U=0.64$ m/s. **a** Original frame shot from a high-speed video. **b** Frame shot after subtracting background. **c** Pixel intensity (pi) distribution along the vertical direction of the frame at different longitudinal location downstream of the roller toe (x–x_{toe} = 0.05, 0.1, 0.15, 0.2, 0.25, 0.3 m)—the black arrows mark the transitions from regions of high to low pixel intensity. **d** Ensemble-averaged vertical profile of the pixel intensity (pi) at different longitudinal location downstream of the roller toe (x–x_{toe} = 0.05, 0.1, 0.15, 0.2, 0.25, 0.3 m)

sampling location $x=8.5$ m. The basic probe output was the instantaneous void fraction c, defined as $c=1$ in air and $c=0$ in water. Typical results are shown in Fig. 6 in terms of the instantaneous liquid fraction $(1-c)$. Considering a probe sensor located at $z/d_1>1$, the phase-detection sensor would be initially located in air and the instantaneous liquid fraction would be zero prior to the bore passage. During the bore passage, the sensor would pierce air-to-water interfaces, water-to-air interfaces, water drops, and bubbly structures, until the liquid fraction would become unity, as long as the sensor elevation z was below the conjugate water elevation. The relative arrival time of the first air-to-water interface

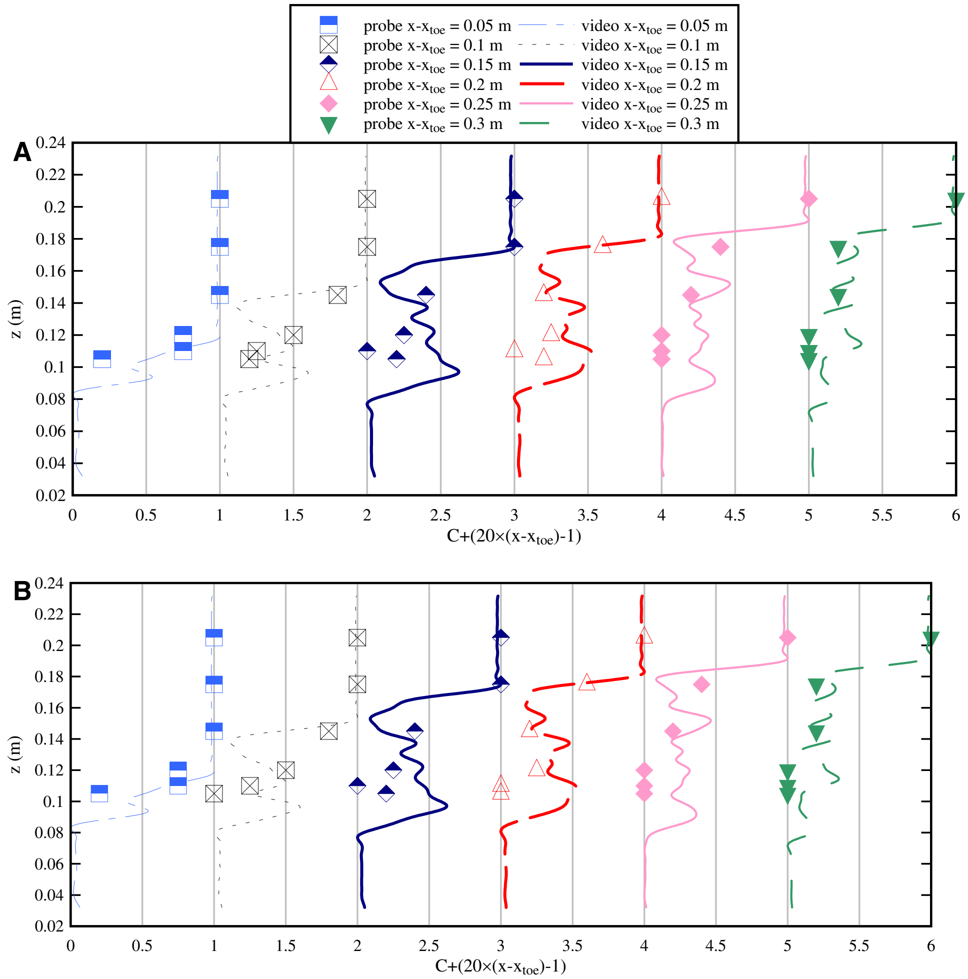

Fig. 5 Ensemble-averaged void fraction analysed from high-speed video movies (smoothed over a window of 20)—comparison to dual-tip phase-detection probe measurements (Probe 1 leading tip) using a 10% threshold (4 V) and a 50% threshold (2.3 V)—flow conditions: $Q = 0.101$ m^3/s, $x = 8.50$ m, $\mathrm{Fr}_1 = 2.18$, $d_1 = 0.097$ m, $U = 0.64$ m/s, the same legend for both graphs. **a** 10% threshold data. **b** 50% threshold

would depend upon the sensor elevation, with increasing delay with increasing elevation above the initial water surface. Figure 6 shows the typical delayed water-interface detection with increasing vertical elevation z, above the reference probe elevation.

The instantaneous vertical distributions of liquid fraction $(1 - c)$ were analysed in terms of the instantaneous clear-water depth (Eq. 4). In Fig. 7, the experimental results are compared with the acoustic displacement meter (ADM) data; namely, the 10%, 25%, 50%, 75%, and 90% percentiles of the ensemble, denoted d_{10}, d_{25}, d_{50}, d_{75}, and d_{90}, respectively. Note the horizontal axis $U \times t$ expressed in meters, with $t = 0$ corresponding to the detection of the first air-to-water interface by the leading sensor of the reference probe (i.e., roller toe). The comparison between the characteristic depth data derived from air–water flow measurements and the acoustic displacement meter (ADM) data indicated that the instantaneous clear-water depth d was about the median ADM depth data d_{50} (Fig. 7). Although the results were obtained in a rapidly varied unsteady flow, the finding was close to observations in stationary hydraulic jumps (Chachereau and Chanson 2011; Wang and Chanson 2015) and in skimming flows on stepped spillway (Felder and Chanson 2014).

The side profile of the breaking bore roller was extracted from the ultra-high-speed movies. Each side profile was smoothed over 22 frames, and Fig. 7 illustrates the ensemble-averaged results over 22 profiles. The high-speed video data showed a better agreement with instantaneous clear-water depth measured by the phase-detection probe array for the front portion of the breaking bore roller ($0 < U \times t < 0.2$ m). Further downstream of the roller toe, the high-speed video data showed a better agreement with the ADMs ($U \times t > 0.2$ m). This indicated intensive aeration occurred typically within 0.2 m downstream of the roller toe for the tested Froude number, with high variability of free-surface deformation and large droplet ejection.

5.2 Ensemble-averaged air–water flow properties

At three-dimensionless vertical elevations along the channel centreline, the phase-detection measurements were repeated between 25 and 50 times, and ensemble-averaged. Basic outputs included the instantaneous ensemble-median liquid

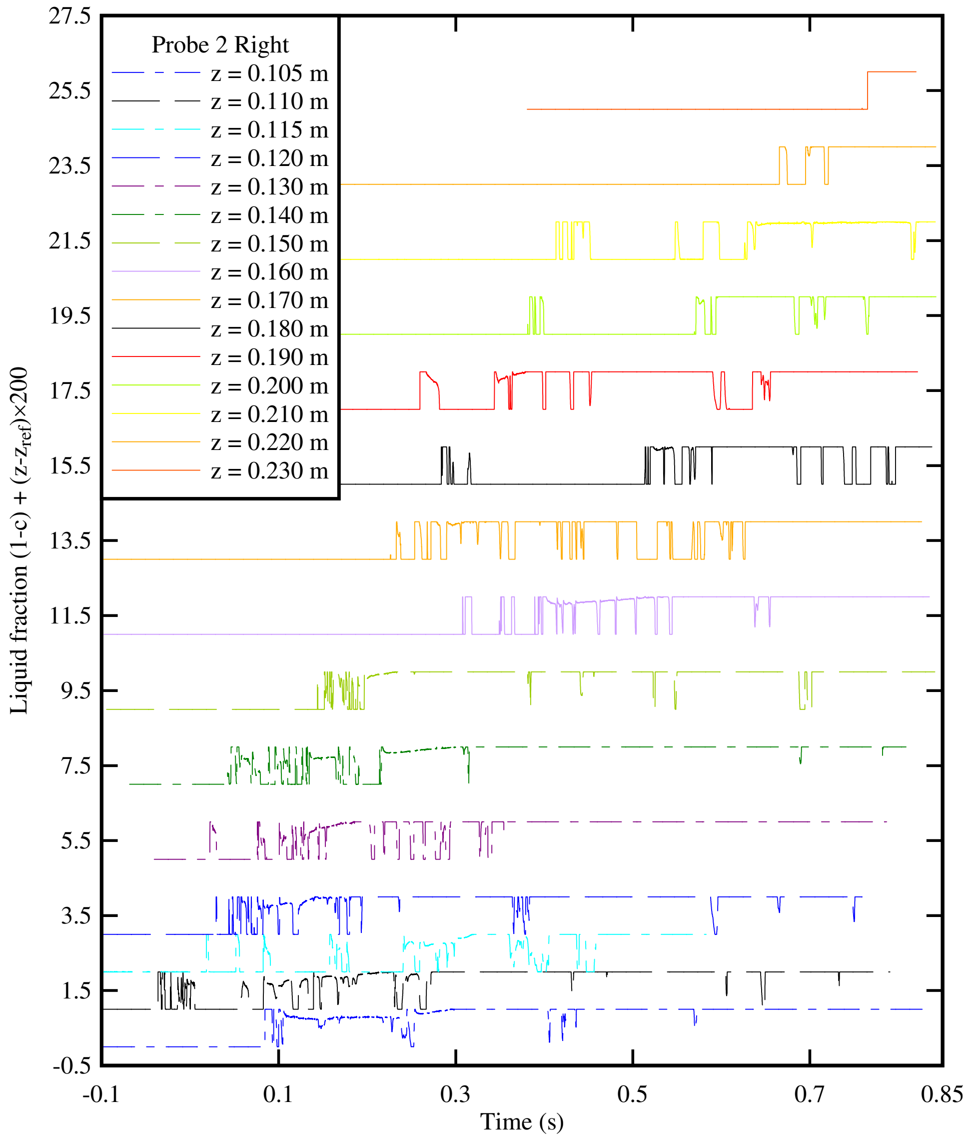

Fig. 6 Time-variation of instantaneous liquid fraction at several elevations—flow conditions: $Fr_1 = 2.18$, $d_1 = 0.097$ m, $U = 0.64$ m/s, Probe 2 (right sensor)

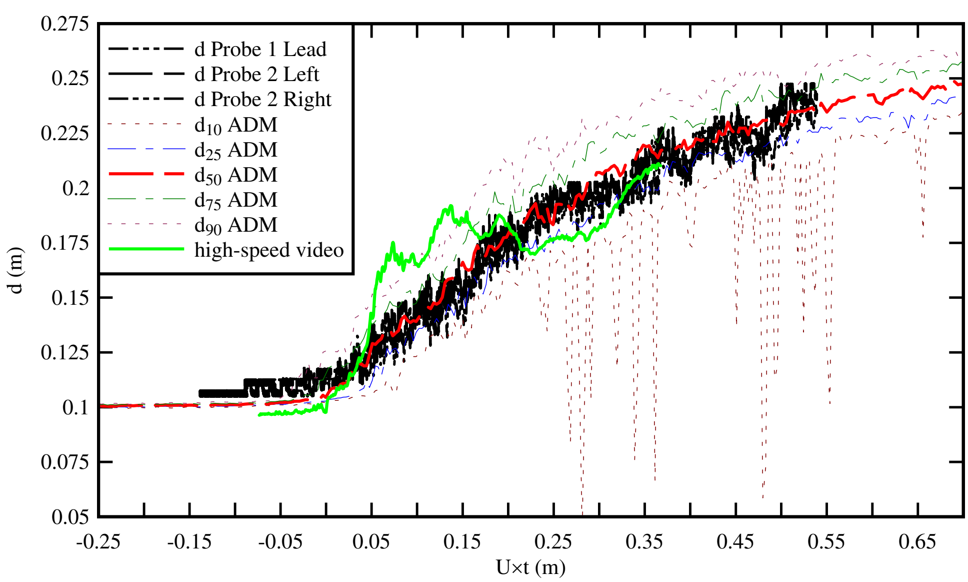

Fig. 7 Comparison between instantaneous clear-water depth *d*, acoustic displacement meter data (10%, 25%, 50%, 75%, 90% percentiles, coloured lines), and ensemble-averaged high-speed video data at $x = 8.50$ m—flow conditions: $x = 8.50$ m, $Fr_1 = 2.18$, $d_1 = 0.097$ m, and $U = 0.64$ m/s

fraction $(1 - C)$, the instantaneous ensemble variance of liquid fraction $(1 - c_{mse})$, and the cumulative number of bubbles N_{ab} for all runs (Sect. 3.2). Figure 8 presents the dimensionless time-variations of instantaneous ensemble-median liquid fraction and instantaneous ensemble variance of liquid fraction, and cumulative number of bubbles N_{ab}.

At a given elevation, the ensemble-median liquid fraction data showed a quasi-monotonic increase in liquid fraction with increasing time. In comparing the data collected at $z/d_1 = 1.08$ and 1.24, the steeper curve at $z/d_1 = 1.08$ corresponded to a lesser aeration of the roller at the reference probe elevation $z/d_1 = 1.08$ (Fig. 8a), in comparison to the data recorded at $z/d_1 = 1.24$ (Fig. 8b). At the highest elevation ($z/d_1 = 1.80$), the liquid fraction data were more scattered, as they corresponded to the upper region the roller and captured water drops, spray, and splashing (Fig. 8c). The time-variation of the liquid fraction variance presented consistently a maximum value about $(1 - c_{mse})_{max} \approx 0.25$ for a liquid fraction $(1 - C) \approx 0.5$. The finding was consistent with the expected parabolic relationship between ensemble-averaged liquid fraction and mean-square error (MSE).

The cumulative number of detected bubbles showed sizeable differences between probe sensors (Fig. 8). While some small difference might be accounted for physical variations between individual probe sensors, it is believed that the data scatter mostly reflected the three-dimensional nature of the air–water roller motion and the in-homogeneity of the turbulent air–water mixture. Although the present data are reported in terms of cumulative number of detected bubbles for all 50 runs (Fig. 8a) or 25 runs (Fig. 8b, c), a probe sensor detected on average between 10 and 15 air–water entities for each single experimental run. That was a fairly small number of air–water interfaces, and air pockets, detected by a fixed probe sensor.

6 Conclusion

Detailed unsteady air–water flow measurements were conducted in a breaking bore propagating in a large-size channel, using an array of dual-tip phase-detection probes ($\varnothing = 0.25$ mm) and an ultra-high-speed video camera (22,000 fps). Experiments were repeated to perform ensemble averaging. The physical data showed a steep roller front, with a very-dynamic air–water bubbly region. Overall, the amount of entrained air was quantitatively small for $Fr_1 = 2.2$. All experimental measurements indicated a relatively limited air–water roller region and the number of air bubbles was tiny, with between 5 and 20 bubbles detected per phase-detection probe sensor at each vertical elevation, within $1.2 < z/d_1 < 2.5$. A relatively simple flow visualisation technique was applied to retrieve the two-dimensional side-looking profile of the roller edge and average void fraction. Results suggested strong

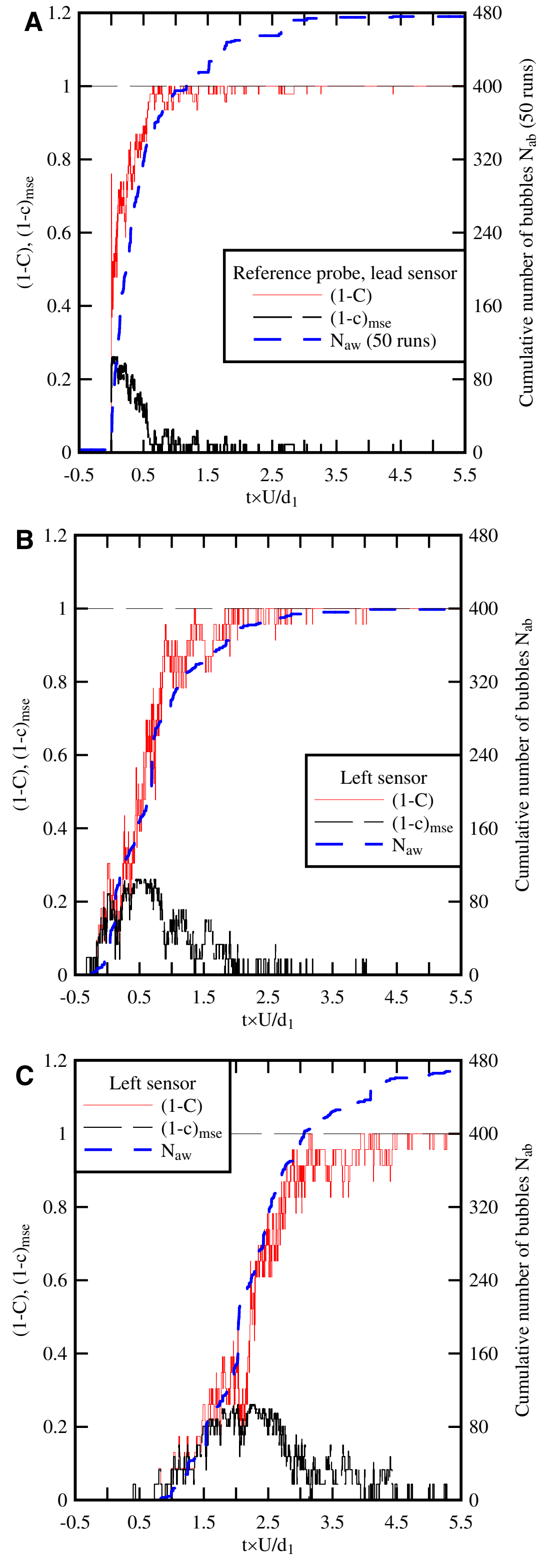

Fig. 8 Instantaneous ensemble-median liquid fraction and liquid fraction variance (mean-square error) at several vertical elevations $z/d_1 = 1.08$, 1.24 and 1.80. **a** $z - z_{ref} = 0$, $z/d_1 = 1.08$, reference probe, lead sensor, 50 runs. **b** $z - z_{ref} = 0.015$ m, $z/d_1 = 1.24$, Probe 2, left sensor, 25 runs. **c** $z - z_{ref} = 0.070$ m, $z/d_1 = 1.80$, Probe 2, left sensor, 25 runs

roller aeration in the close vicinity of the roller toe, specifically 0.05–0.15 m downstream of the toe.

The air–water interface detections presented of lot of data scatter and randomness, linked to the three-dimensional nature of the air–water roller motion, and evidenced of the in-homogeneity of the turbulent air–water mixture. With all flow visualisation techniques, the results must be validated independently. In the present study, a phase-detection probe was used to validate the video movie results. The probe data, however, lacked spatial variability and the repeats were limited to five runs, due to time constraint. Future visual studies of breaking bores could benefit with a more complete data set, with probes placed throughout the transverse flow width and along the roller, with the experimental repeats of at least 25 runs at each vertical elevation. The present study reinforces the needs of high-quality validation data set, together with a refined data processing technique that can be used for advanced instrument, such as the ultra-high-speed video camera.

Acknowledgements The authors would like to thank Dr Hubert Branger (IRPHE, University of Marseille, France) and Dr Jorge Leandro (Technical University of Munich, Germany) for their detailed review of the report and valuable comments. They acknowledge the helpful inputs of Professor Pierre Lubin (University of Bordeaux, France) and Dr Hang Wang (The University of Queensland, Australia), as well as discussions with Dr Gangfu Zhang (The University of Queensland, Australia) and Dr Matthias Kramer (The University of Queensland, Australia). The authors thank the reviewers for their helpful and constructive comment. The technical assistance of Jason Van Der Gevel and Stewart Matthews (The University of Queensland, Australia) is greatly appreciated.

Appendix 1: Video movies

Two high-speed video movies are provided as supplementary materials. Their details and characteristics are summarised below.

Finame	Description	Native movie format	Video movie details
bore_probe_test8.avi	Three-quarter view of advancing bore passing the phase-detection probe array about the channel centreline	20,000 fps. Full HD (1280 × 800 pixels)	Frame rate: 200 fps replayed at 5 fps. Full HD movie (1280 × 800 pixels). Duration: 14 s
bore-side.avi	Side view of advancing bore	22,607 fps. Full HD (1280 × 800 pixels)	Frame rate: 226 fps replayed at 30 fps. Full HD movie (1280 × 800 pixels). Duration: 15 s

Appendix 2: Relationship between pixel intensity and void fraction in a breaking bore roller

In a disperse bubbly flow, a relationship between pixel intensity and bubble density may be derived from Lambert's law on light transmission intensity (Shamoun et al. 1999):

$$Ln\left(\frac{pi}{pi_o}\right) \propto -\frac{\partial N_{ab}}{\partial t} \tag{9}$$

where $\mathrm{pi_o}$ is a reference pixel intensity, N_{ab} is the cumulative number of detected bubbles, and t is the time. $\partial N_{\mathrm{ab}}/\partial t$ is implicitly an instantaneous bubble count rate. The above expression for the transmittance may be re-arranged in terms of the void fraction for disperse spherical bubbles:

$$\frac{\mathrm{pi}}{\mathrm{pi}_o} = \mathrm{e}^{-K\,C} \tag{10}$$

with C the void fraction and K a constant. Equation (10) was successfully validated for low void fractions, i.e., typically well below 0.20, against gas hold up data in water column and void fraction data beneath breaking wave (Shamoun et al. 1999; Leppinen and Dalziel 2001; Kimmoun and Branger 2007). For completeness, optical flow methods applied to free-surface air–water flows showed recently that the bubble count rate was correlated negatively to luminance standard deviation (Zhang and Chanson 2018).

In the present study, the void fraction was estimated as a linear function of the pixel intensity, following Mossa and Tolve (1998) and Leandro et al. (2012). Both studies were conducted in free-surface flows, with complete vertical distributions of void fractions ranging from close to zero up to unity, above the free-surface of a hydraulic jump roller. For the present experiments, the relationship between pixel intensity and void fraction was checked, using the data

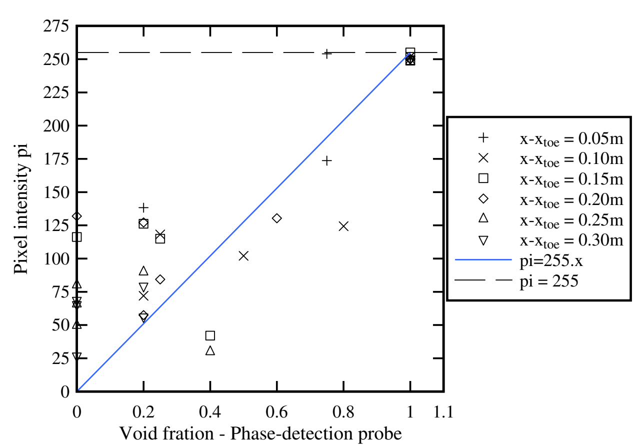

Fig. 9 Relationship between pixel intensity and void fraction in a breaking bore roller—data corresponding to Fig. 5a of this article

presented in Fig. 5a. The results are presented in Fig. 9. Despite the data scatter, linked to the small number of phase-detection probe measurements (six locations) and limited number of repetitions (5), the results showed a monotonic increase in pixel intensity with increasing void fraction from zero to unity. In Fig. 9, the data were correlated to a linear fit with a normalised correlation coefficient of 0.75 and a standard error of 54.1.

References

Bradshaw P (1971) An introduction to turbulence and its measurement. In: The Commonwealth and International Library of Science and technology Engineering and Liberal Studies. Thermodynamics and Fluid Mechanics Division. Pergamon Press, Oxford, p 218

Brocchini M, Peregrine DH (2001) The dynamics of strong turbulence at free surfaces. Part 2. Free-surface boundary conditions. J Fluid Mech 449:255–290

Cartellier A, Achard JL (1991) Local phase detection probes in fluid/fluid two-phase flows. Rev Sci Instrum 62(2):279–303

Chachereau Y, Chanson H (2011) Bubbly flow measurements in hydraulic jumps with small inflow froude numbers. Int J Multiph Flow 37(6):555–564. https://doi.org/10.1016/j.ijmultiphaseflow.2011.03.012

Chanson H (1997) Air bubble entrainment in free-surface turbulent shear flows. Academic Press, London, p 401

Chanson H (2002) Air–water flow measurements with intrusive phase-detection probes. Can we improve their interpretation?. J Hydraul Eng ASCE 128(3):252–255. https://doi.org/10.1061/(ASCE)0733-9429(2002)128:3(252)

Chanson H (2004) Unsteady air–water flow measurements in sudden open channel flows. Exp Fluids 37(6):899–909. https://doi.org/10.1007/s00348-004-0882-3

Chanson H (2005) Air–water and momentum exchanges in unsteady surging waters: an experimental study. Exp Thermal Fluid Sci 30(1):37–47. https://doi.org/10.1016/j.expthermflusci.2005.03.017

Chanson H (2013) Hydraulics of aerated flows: qui pro quo?. J Hydraul Res 51(3):223–243. https://doi.org/10.1080/00221686.2013.795917

Chanson H (2016) Phase-detection measurements in free-surface turbulent shear flows. J Geophys Eng 13(2):S74–S87. https://doi.org/10.1088/1742-2132/13/2/S74

Chanson H, Brattberg T (2000) Experimental study of the air–water shear flow in a hydraulic jump. Int J Multiph Flow 26(4):583–607. https://doi.org/10.1016/S0301-9322(99)00016-6

Chanson H, Docherty NJ (2012) Turbulent velocity measurements in open channel bores. Eur J Mech B Fluids 32:52–58. https://doi.org/10.1016/j.euromechflu.2011.10.001

Chanson H, Aoki S, Hoque A (2006) Bubble entrainment and dispersion in plunging jet flows: freshwater versus seawater. J Coast Res 22(3):664–677. https://doi.org/10.2112/03-0112.1

Coakley DB, Haldeman PM, Morgan DG, Nicolas KR, Penndorf DR, Wetzel LB, Weller CS (2001) Electromagnetic scattering from large steady breaking waves. Exp Fluids 30(5):479–487

Cointe R, Tulin MP (1994) A theory of steady breakers. J Fluid Mech 276:1–20

Cox DT, Shin S (2003) Laboratory measurements of void fraction and turbulence in the bore region of surf zone waves. J Eng Mech ASCE 129(10):1197–1205

Duncan JH (1981) An experimental investigation of breaking waves produced by a towed hydrofoil. Proc R Soc Lond A 377:331–348

Felder S, Chanson H (2014) Air–water flows and free-surface profiles on a non-uniform stepped chute. J Hydraul Res IAHR 52(2):253–263. https://doi.org/10.1080/00221686.2013.841780

Felder S, Chanson H (2015) Phase-detection probe measurements in high-velocity free-surface flows including a discussion of key sampling parameters. Exp Thermal Fluid Sci 61:66–78. https://doi.org/10.1016/j.expthermflusci.2014.10.009

Herringe RA, Davis MR (1974) Detection of instantaneous phase changes in gas–liquid mixtures. J Phys E Sci Instrum 7:807–812

Hoque A, Aoki S (2005) Distributions of void fraction under breaking waves in the surf zone. Ocean Eng 32(14–15):829–1840

Hornung HG, Willert C, Turner S (1995) The flow field downstream of a hydraulic jump. J Fluid Mech 287:299–316

Hoyt JW, Sellin RHJ (1989) Hydraulic jump as 'mixing layer'. J Hydraul Eng ASCE 115(12):1607–1614

Hwung HH, Chyan JM, Chung YC (1992) Energy dissipation and air bubbles mixing inside surf zone. In: Proceedings of 23rd international conference on coastal engineering, Venice ASCE, Italy, vol 1, Chap 22, pp 308–321

Jones OC, Delhaye JM (1976) Transient and statistical measurement techniques for two-phase flows: a critical review. Int J Multiph Flow 3:89–116

Kimmoun O, Branger H (2007) A particle image velocimetry investigation on laboratory surf-zone breaking waves over a sloping beach. J Fluid Mech 588:353–397

Leandro J, Carvalho R, Chachereau Y, Chanson H (2012) Estimating void fraction in a hydraulic jump by measurements of pixel intensity. Exp Fluids 52(5):1307–1318. https://doi.org/10.1007/s00348-011-1257-1

Leng X (2018) Study of turbulence: the unsteady propagation of bores and surges. Ph.D. Thesis, School of Civil Engineering, The University of Queensland, Brisbane, Australia, p 364, 2 Digital Appendices. https://doi.org/10.14264/uql.2018.501

Leng X, Chanson H (2015a) Turbulent advances of a breaking bore: preliminary physical experiments. Exp Thermal Fluid Sci 62:70–77. https://doi.org/10.1016/j.expthermflusci.2014.12.002

Leng X, Chanson H (2015b) Unsteady turbulence in expansion waves in rivers and estuaries: an experimental study. Environ Fluid Mech 15(5):905–922. https://doi.org/10.1007/s10652-014-9385-9

Leng X, Chanson H (2017) Unsteady velocity profiling in bores and positive surges. Flow Meas Instrum 54:136–145. https://doi.org/10.1016/j.flowmeasinst.2017.01.004

Leng X, Chanson H (2018) Two-phase flow characteristics of a breaking tidal bore roller: microscopic properties. Hydraulic Model Report No. CH109/18, School of Civil Engineering, The University of Queensland, Brisbane, Australia, p 190 **(ISBN 978-1-74272-195-8)**

Leppinen DM, Dalziel SB (2001) A light attenuation technique for void fraction measurement of microbubbles. Exp Fluids 30:214–220

Liu TJ, Bankoff SG (1993) Structure of air–water bubbly flow in a vertical pipe—II. Void fraction, bubble velocity and bubble size distribution. Intl J Heat Mass Transfer 36(4):1061–1072

Lubin P, Chanson H (2017) Are breaking waves, bores, surges and jumps the same flow?. Environ Fluid Mech 17(1):47–77. https://doi.org/10.1007/s10652-016-9475-y

Misra SK, Thomas M, Kambhamettu C, Kirby JT, Veron F, Brocchini M (2006) Estimation of complex air–water interfaces from particle image velocimetry images. Exp Fluids 40:764–775

Mossa M, Tolve U (1998) Flow visualization in bubbly two-phase hydraulic jump. J Fluids Eng 120:160–165

Murai Y, Oishi Y, Takeda Y, Yamamoto F (2006) Turbulent shear stress profiles in a bubbly channel flow assessed by particle tracking velocimetry. Exp Fluids 41:343–352

Piquet J (1999) Turbulent flows. Models and physics. Springer, Berlin, p 761

Rajaratnam N (1962) An experimental study of air entrainment characteristics of the hydraulic jump. J Inst Eng India 42(7):247–273

Schlichting H, Gersten K (2000) Boundary layer theory, 8th edn. Springer, Berlin, p 707

Shamoun B, Beshbeeshy M, Bonazza R (1999) Light extinction technique for void fraction measurements in bubbly flow. Exp Fluids 26:16–26

Spiegel MR (1972) Theory and problems of statistics. McGraw-Hill Inc., New York

Stutz B, Reboud JL (1997) Experiments in unsteady cavitation. Exp Fluids 22:191–198

Stutz B, Reboud JL (2000) Measurements within unsteady cavitation. Exp Fluids 29:545–552

Toombes L (2002) Experimental study of air–water flow properties on low-gradient stepped cascades. Ph.D. Thesis, Department of Civil Engineering, The University of Queensland, Brisbane, Australia

Tricker RAR (1965) Bores, breakers, waves and wakes. American Elsevier Publ. Co., New York

Wang H, Chanson H (2015) Experimental study of turbulent fluctuations in hydraulic jumps. J Hydraul Eng ASCE 141(7):10. https://doi.org/10.1061/(ASCE)HY.1943-7900.0001010 **(Paper 04015010)**

Wang H, Leng X, Chanson H (2017) Bores and hydraulic jumps. Environmental and geophysical applications. Engineering and computational mechanics, Proceedings of the Institution of Civil Engineers, UK, vol 170, no. EM1, pp 25–42. https://doi.org/10.1680/jencm.16.00025

Wood IR (1984) Air entrainment in high speed flows. In: Proceedings of international symposium on scale effects in modelling hydraulic structures, IAHR, Esslingen, Germany, H. KOBUS editor, paper 4.1, p 7

Wood IR (1985) Air water flows. In: Proceedings of 21st IAHR congress, Melbourne, Australia, Keynote address, pp 18–29

Wood IR (1991) Air entrainment in free-surface flows. In: IAHR hydraulic structures design manual No. 4. Hydraulic Design Considerations, Balkema Publ., Rotterdam, p 149

Zhang G, Chanson H (2018) Application of local optical flow methods to high-velocity free-surface flows: validation and application to stepped chutes. Exp Thermal Fluid Sci 90:186–199. https://doi.org/10.1016/j.expthermflusci.2017.09.010